Elucidation of Iron Gettering Mechanisms in Boron-Implanted Silicon Solar Cells

Hannu S. Laine [ID], Ville Vähänissi, Zhengjun Liu [ID], Ernesto Magaña, Jan Krügener, Ashley E. Morishige [ID], Kristian Salo, Barry Lai, Hele Savin, and David P. Fenning [ID]

Abstract—To facilitate cost-effective manufacturing of boron-implanted silicon solar cells as an alternative to BBr$_3$ diffusion, we performed a quantitative test of the gettering induced by solar-typical boron-implants with the potential for low saturation current density emitters (<50 fA/cm^2). We show that depending on the contamination level and the gettering anneal chosen, such boron-implanted emitters can induce more than a 99.9% reduction in bulk iron point defect concentration. The iron point defect results as well as synchrotron-based nano-X-ray-fluorescence investigations of iron precipitates formed in the implanted layer imply that, with the chosen experimental parameters, iron precipitation is the dominant gettering mechanism, with segregation-based gettering playing a smaller role. We reproduce the measured iron point defect and precipitate distributions via kinetics modeling. First, we simulate the structural defect distribution created by the implantation process, and then we model these structural defects as heterogeneous precipitation sites for iron. Unlike previous theoretical work on gettering via boron- or phosphorus-implantation, our model is free of adjustable simulation parameters. The close agreement between the model and experimental results indicates that the model successfully captures the necessary physics to describe the iron gettering mechanisms operating in boron-implanted silicon. This modeling capability allows high-performance, cost-effective implanted silicon solar cells to be designed.

Index Terms—Boron implantation, gettering, iron, silicon, simulation.

I. INTRODUCTION

GETTERING, or mitigating the effects of deleterious trace impurities, is a key element of silicon solar cell processing. Typical feedstock materials contain 10^{11}–10^{15} cm^{-3} of most transition metals [1], which are highly detrimental to minority charge carrier lifetime and limit device efficiency potential. Within the photovoltaics (PV) industry, there is a strong interest to switch from the dominant p-type substrates into n-type substrates, mostly due to longer minority carrier diffusion lengths in n-type substrates that can enable higher cell efficiencies [2], [3]. Despite the longer diffusion lengths, defect-related bulk recombination still contributes to performance limits of high-efficiency n-type silicon solar cell architectures [4]–[6]. Optimal gettering strategies for boron-doped emitters are needed so that bulk lifetime can be maximized for the final cell.

Of the various boron doping methods, ion-implantation offers a unique compromise to achieve low emitter recombination and high-quality surface passivation, while enabling reasonable throughput and good process control, single-sided doping [7], facile co-doping of phosphorus and boron [8], and avoiding high near-surface concentrations and the boron rich layer (BRL) [9], [10]. A significant fraction of the body of research on transition metal gettering in silicon revolves around iron, because its prevalence [11], easy characterization [12], [13] and relative similarity in diffusivity and solubility [14] to other transition metals make iron a "model" fast-diffusing transition metal. Previous research on iron gettering via boron doping has established that regardless of the doping method (implantation [15]–[18], solid-state diffusion [19]–[22], BBr$_3$ diffusion [23]–[25], or epitaxy [26]–[28]), negative boron atoms pair with positive interstitial iron atoms to induce a segregation of iron point defects toward the highly boron-doped layer. This segregation is most effective at low temperatures [17], [28] (<400 °C), when the diffusion length of dissolved iron and several other transition metal point defects is limited [13], which limits its applicability in solar cell processing. Additionally, possible inactive boron [18]–[22] and the BRL [24] seem to act as a precipitation site for iron point defects, which can greatly enhance the bulk iron point defect reduction. However, inactive boron and the BRL

induce recombination and thus are preferably avoided in the manufacturing of high-efficiency solar cells [7]. It is also known that ion-implantation disturbs the silicon lattice generating silicon interstitials [29]. Upon high-temperature annealing, these interstitials can evolve into dislocation loops and other structural defects generally referred to as "implantation damage" [29]–[31]. Implantation damage has been used as a favorable precipitation site and thus an effective sink for iron point defects [15], [16], [31]–[35], but no studies have used boron-implant parameters typical to the solar cell industry (<20 keV energy, ~10^{15} cm^{-2} dose).

Here, we systematically study iron gettering with low-energy PV-relevant boron implanted emitters using two controlled iron contamination levels. We identify precipitation of iron in the implanted layer microscopically via synchrotron-based X-ray-fluorescence. To elucidate the dominant gettering mechanisms, we reproduce the experimental results via simulation. Previous theoretical studies on iron precipitation at either implanted boron or phosphorus layers, including by the authors, have "fit" their experimental results by using the precipitation site density and radius as free parameters [15], [16], [35]. Because different implantation parameters induce different implant damage distributions [29]–[31], such free parameters limit the generalizability of the fitted results over different implant parameters and implant anneals. Here, we explicitly model the implantation damage distribution and its response to post-implant high-temperature processing and hence avoid using any free parameters in the simulations. The avoidance of free parameters facilitates predictive modeling of the residual iron distribution in the final solar cell, based on implantation parameters, iron contamination level, and thermal budget alone. Such models for phosphorus diffusion gettering [36]–[42] have accelerated cycles of learning in p-type silicon solar cells, which are the norm of the silicon solar cell industry today [2]. The validated model here for boron gettering can be applied in future n-type solar cell processing.

II. IRON GETTERING EXPERIMENTS AND QUANTIFICATION

We use polished, <100> oriented, 390 ± 10 μm thick, 3–5 Ωcm resistivity, 100 mm diameter, low-oxygen content (<10 ppma), electronic-grade p-type Cz-wafers. We use p-type substrates in order to easily characterize iron point defect concentration. Iron behaves similarly in n- and p-type substrates at relevant process temperatures, because silicon is largely intrinsic at temperatures above 400 °C [43], making our results descriptive of both p- and n-type substrates. Because the gettering efficiency of implanted emitters is known to heavily depend on iron contamination level [35], [44] we use two different, controlled contamination levels. We intentionally contaminate [45] the wafers with iron by immersing them into a spiked Standard Clean (SC)-1 solution and anneal them at 1) 845 °C for 55 min for a "low" contamination level of $[Fe_0] = 3.0 \times 10^{13}$ cm^{-3} or 2) 945 °C for 45 min for a "high" contamination level of $[Fe_0] = 2.4 \times 10^{14}$ cm^{-3}.

After iron contamination, the wafers are boron-implanted with a dose of 3×10^{15} cm^{-2}, energy of 10 keV and 7° tilt. The wafers experience SC-1 and SC-2 cleans and a diluted HF-dip, and the dopants are driven-in, the implant damage healed

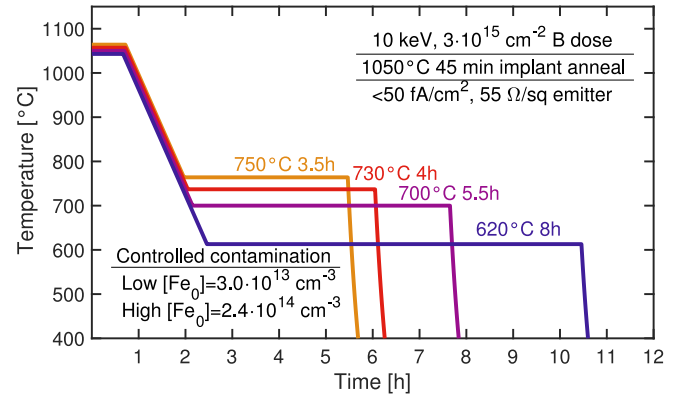Fig. 1.   Gettering anneals and experimental parameters.

and the wafer surfaces oxidized by annealing the wafers at 1050 °C for 45 min, which included 20 min of annealing in an oxidizing ambient. A previous study [46] with identical implant parameters on n-type substrates showed these implants to have an emitter saturation current density (j_{0e}) potential below 50 fA/cm^2, making them relevant for high-efficiency solar cell processing. To test gettering efficiency as a function of applied thermal budgets, the implant anneal was directly followed by a 4 °C/min ramp down to a gettering anneal at 1) 750 °C for 3.5 h, 2) 730 °C for 4 h, 3) 700 °C for 5.5 h, or 4) 620 °C for 8 h. After the gettering anneals, the furnace ejects the wafers directly to room temperature, with an estimated cool-down rate of 4 °C/s [47]. The gettering times are chosen to ensure a $\sqrt{Dt}$ interstitial iron diffusion length of at least twice the wafer thickness, facilitating significant changes in the iron distribution at the gettering temperature. Thick wafers are used here to ensure accurate measurements of the diffusion length via surface photovoltage (SPV). For thinner wafers, the dwell times can be shortened while maintaining similar gettering efficiencies. The gettering anneals, as well as other experimental parameters, are summarized in Fig. 1.

Additionally, two kinds of reference wafers were made. First, to investigate possible internal gettering via iron precipitation in the wafer bulk during the gettering anneals, contaminated reference samples without any boron-implantation were included in the 750 °C and 620 °C gettering anneals. These samples showed no measurable changes in the bulk iron concentration (cf., Fig. 2), which suggests that all changes induced to the iron point defect concentration in the implanted samples are caused by the B-implantation process itself, and bulk precipitation or gettering via surface dielectrics [48], [49] are not considered in the simulations of this study. When comparing these nonimplanted samples to previous gettering studies without an extrinsic gettering layer, it is important to note that here, there was no room temperature step between the high-temperature implant anneal and the gettering anneal, which would have likely promoted bulk precipitation [50]. Second, to investigate possible boron precipitation or additional boron diffusion during the low-temperature anneals, boron-implanted, n-type reference wafers were included in the 750 °C and 620 °C gettering anneals and one was directly ramped down to 700 °C after implant activation and pulled out of the furnace. The sheet resistances of these
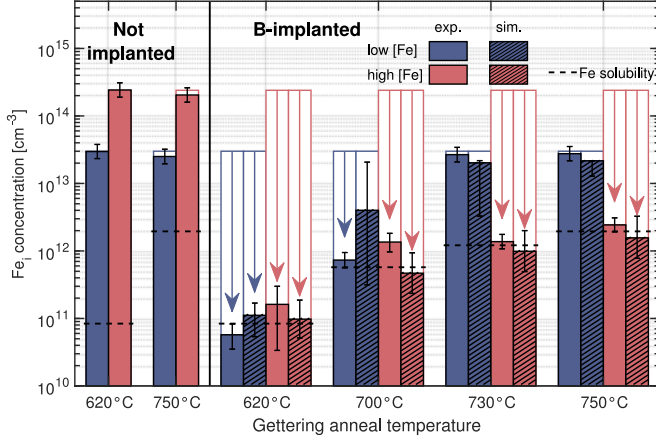
Fig. 2. Experimental (solid bars) and simulated (hashed bars) gettering efficiencies for the gettering anneals in the lowly contaminated (blue bars) and highly contaminated (red bars) samples, along with their associated uncertainties. The iron solubility at the gettering temperature [54], [55] is shown as a black dashed line and initial iron contamination level as white bars. The experimental point defect results were also discussed in [56].

n-type reference wafers were all 55 Ω/sq. to within the measurement accuracy of the four-point probe used ($\sim$5%), suggesting that the boron distribution is comparable in all the samples.

The iron point defect reduction during the gettering anneals was characterized with the SPV technique, similarly as described in [45]. The charge separation required for the SPV measurement is facilitated by corona charging the oxide on the nonimplanted side of the wafers with $+640\,\mathrm{nC/cm^2}$. To quantify the precipitate size distribution formed within the implanted layer, synchrotron-based nano-X-ray fluorescence (Nano-XRF) was performed at the Advanced Photon Source beamline 2-ID-D with a beam spot size of 210 nm and beam energy of 10 or 13.6 keV. We used a fast 50 ms per-pixel dwell time facilitated by the recently developed fly-scan method [51] to collect a significantly larger statistical dataset than previously in a similar study investigating iron gettering with phosphorus implantation [35]. Other measurement conditions and data quantification procedures were identical to the previous study [35].

III. PREDICTIVE GETTERING MODEL

To simulate both the residual bulk iron point defect concentration as well as the iron precipitate size distribution in the implanted layer, we use as inputs the implantation parameters, the time-temperature profile of the gettering anneal, and the iron contamination level. Our model contains the following three parts.

1) An implantation damage model, which describes the formation of silicon interstitials during ion-implantation and their evolution into dislocation loops during subsequent thermal processing [52].

2) A heterogeneous iron precipitation model, which describes the nucleation and growth of iron precipitates at the implantation damage [53].

3) A segregation model, which describes iron pairing with boron, which increases the solubility of iron in the heavily

boron-doped layer, reducing bulk iron point defect concentration [28].

The uncertainty of the simulated values is estimated by changing the iron solid solubility to lower or higher by a factor of 2, which corresponds to the scatter in the literature data of iron solubility [54], [55]. Further details of the model are included in Appendix A. We stress that no simulation parameters have been fit to the experimental results. To elucidate the relative differences of the segregation-based gettering mechanism and the precipitation-based gettering mechanism, simulations are performed both with and without an active segregation-based gettering mechanism.

IV. RESULTS

A. Experimental and Simulated Bulk Iron Point Defect Concentrations

The experimental bulk iron point defect reductions (gettering efficiencies) induced by the different anneals show trends that can be expected from precipitation-based gettering (cf., Fig. 2). In the highly contaminated samples, the iron concentration decreases in each close to the solid solubility limit, C_S, at the gettering temperature. As is expected in precipitation-dominated gettering, the lowly contaminated samples exhibit a lower gettering efficiency because the supersaturation of iron is lower in these samples and hence the precipitation process is not as strong. The iron concentration in the lowly contaminated samples remains unchanged within measurement accuracy in the 730 °C and 750 °C samples, but is then reduced to approximately the solid solubility limit in the 620 °C and 700 °C samples. The fact that the iron concentration is never observed to be significantly below the solid solubility limit at the gettering temperature further suggests that precipitation is the dominant mechanism.

The simulated gettering efficiencies (with both segregation- and precipitation-based gettering included) shown in Fig. 2 (hashed bars) exhibit similar values to the corresponding experimental ones (solid bars) within the measurement and simulation uncertainty. Furthermore, the simulated values show that, in certain cases, precipitation-based gettering is very predictable: Once a high enough supersaturation is reached, precipitation begins and then proceeds to the solid solubility at the gettering temperature. On the other hand, predicting the exact supersaturation needed can be difficult, as is shown by the large (1–1.5 orders of magnitude) uncertainty in the simulated final $[\mathrm{Fe_i}]$ concentration in the lowly contaminated 700 °C and 730 °C samples. In these samples, precipitation begins, but not strongly enough to necessarily proceed all the way to the solid solubility limit. In this regime, the final simulated bulk $[\mathrm{Fe_i}]$ value is particularly sensitive to uncertainty in the simulation parameters. For all other samples, the uncertainty is within a factor of 2, which is directly related to the experimental uncertainty in the iron solid solubility [54], [55]. Overall, the fact that the simulated and measured $[\mathrm{Fe_i}]$ values agree to within uncertainty for all samples suggests that the essential physical processes are captured within the model, and the model can be used for
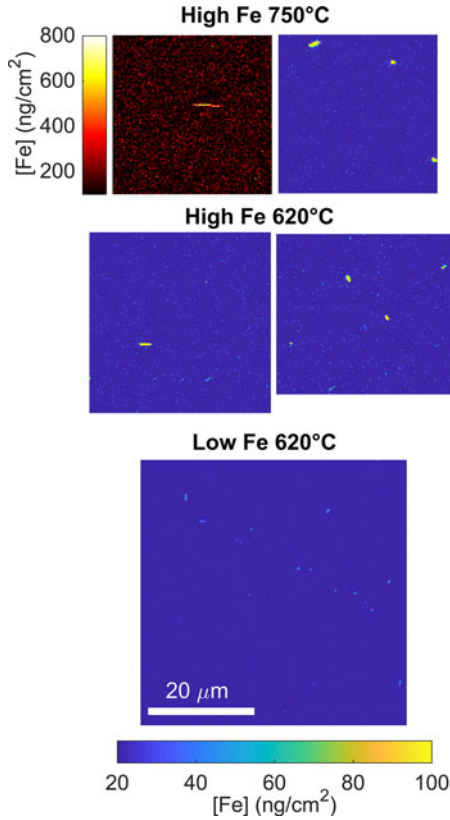
Fig. 3. Quantified Fe K_α fluorescence load in three samples. The left map of the High Fe 750 °C sample was acquired using 13.6 keV incident beam energy, which results in higher noise floor, and is thus displayed on a different color scale and colormap. Another 484 μm^2 were mapped from high Fe 750 °C sample, which did not reveal any precipitates.

predictive simulations with arbitrary implantation parameters, iron contamination levels, and thermal budgets.

B. Experimental and Simulated Iron Precipitate Size Distribution in the Implanted Layer

In addition to quantifying the bulk residual iron point defect concentration, it is important to know and compare the iron precipitate size distribution in the implanted layer. From a device perspective, large precipitates can shunt the pn-junction [57]–[59] and act as a source of point-defects at later stages of high-temperature processing [60], [61], exhibiting a size-dependent [62] dissolution rate. From a theoretical perspective, detecting precipitates and measuring the size distribution elucidates the dominant gettering mechanisms. To test the effect of different contamination level and gettering anneals, while also maximizing the productivity of limited-access synchrotron facilities, three samples were chosen for Nano-XRF measurements: the highly- and lowly contaminated 620 °C samples and the highly contaminated 750 °C sample.

Fig. 3 shows the quantified Fe maps of the three measured samples with iron precipitates observed in each sample. Because the nonimplanted samples showed no detectable change in iron point defect concentration and previous work on P-implanted emitters detected iron within the implanted layer via SIMS
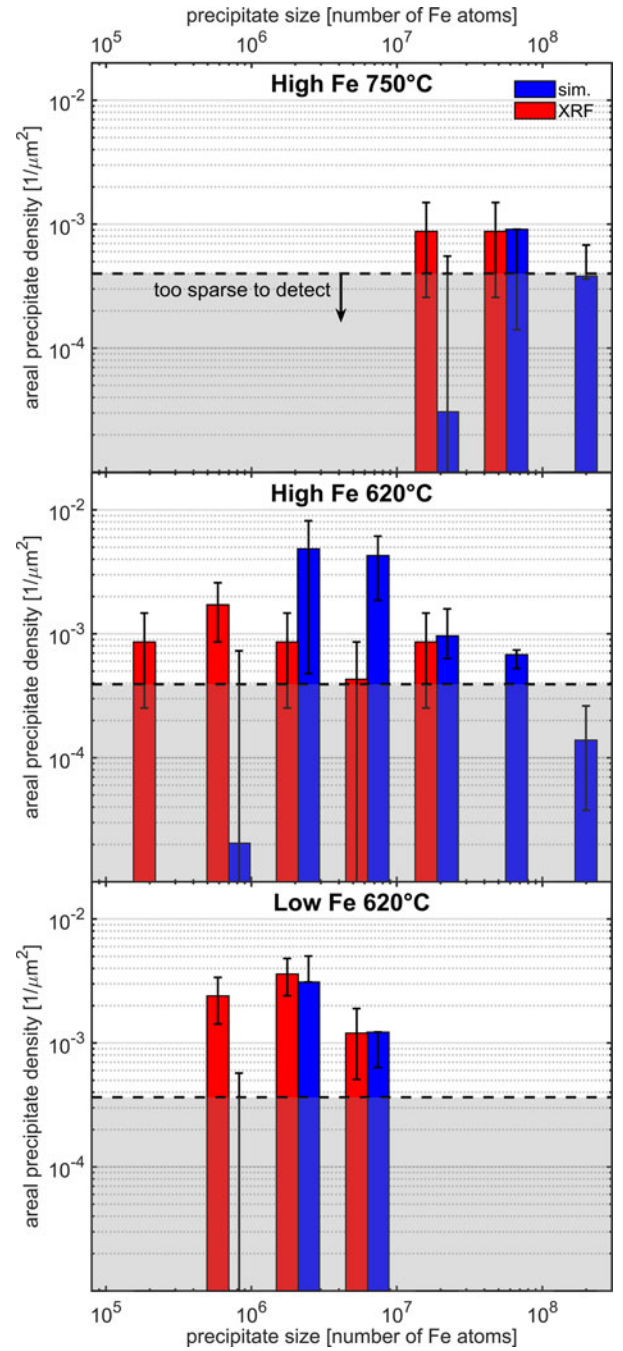
Fig. 4. Simulated ("sim.") and measured ("XRF") precipitate size distributions (blue and red bars, respectively) for the highly contaminated 750 °C and the highly- and lowly contaminated 620 °C samples. The dashed horizontal line describes the minimum detectable density, below which the precipitates are too sparse for a single precipitate to be detected within the mapped area. The size of each measured precipitate is listed separately in Table SI.

[44], we can reasonably conclude that the Fe signal comes from within the implanted layer, implying that precipitation-based gettering is active. The measured samples reveal large (>1 μm in length), anisotropic, needle-like precipitates, similar to what has been observed previously in phosphorus-implanted, iron-contaminated samples [35] and on prebreakdown sites in multicrystalline silicon solar cells [57]. Fig. 4 presents the measured

Fig. 5. Simulated [Fe_i] reductions using the full model ("sim: seg. + prec.") as well as simulating only precipitation and excluding segregation ("sim: prec. only") compared with experimental ("exp.") values. The iron solubility at the gettering temperature [54], [55] is shown as a black dashed line and initial iron contamination level as white bars.

and simulated precipitate size distributions for all three samples. In the 750 °C sample, the precipitates are distinctly larger than in the 620 °C samples in both the simulations and experi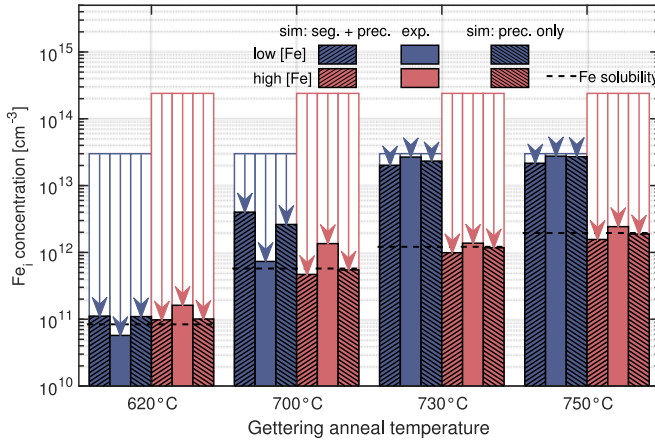ments. This behavior is expected from iron precipitation. At 750 °C, iron solubility is higher than at 620 °C, which slows nucleation. Hence, the 620 °C sample forms a larger number of precipitates. Even though a larger fraction of iron is gettered to the implanted layer in the 620 °C sample, individual precipitates grow larger in the 750 °C sample due to the lower density of precipitates in that sample. Similarly, the precipitates are, on average, smaller in the lowly contaminated 620 °C sample than in the highly contaminated sample because the lowly contaminated sample contains less iron.

When examining the agreement between experimental and simulated size distributions, we note that distributions of the highly contaminated 750 °C sample and lowly contaminated 620 °C sample are consistent within measurement and simulation accuracy. The highly contaminated 620 °C sample is an exception, with error bars not overlapping for three different sizes (bars), which suggest that other sources of uncertainty are present. These sources could be, for example, uncertainty in the measured precipitate sizes via XRF, which can be up to a factor of two [63], or uncertainty in the simulated dislocation loop density, which can similarly be up to a factor of two. Across all samples, there is a tendency for the simulations to predict slightly larger precipitates at a slightly lower density than what is experimentally observed. This suggests that the physical precipitation site density is more likely to be lower, rather than higher, than the simulated value.

V. DISCUSSION: RELATIVE STRENGTH OF SEGREGATION- AND PRECIPITATION-BASED GETTERING AS A FUNCTION OF IRON CONCENTRATION

The simulated bulk [Fe_i] results (cf., Fig. 2), as well as precipitate size distributions (cf., Fig. 4) were reproduced
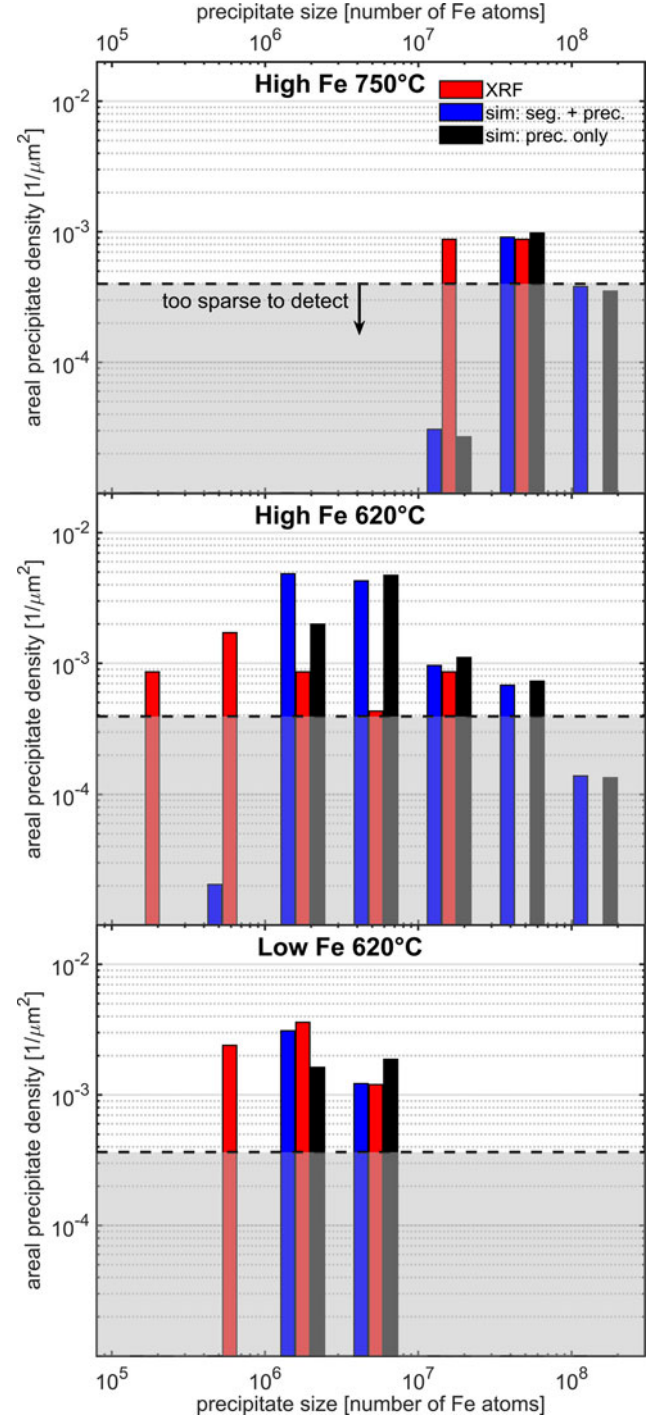
Fig. 6. Simulated size distribution using the full model ("sim: seg. + prec.") as well as simulating only precipitation and excluding segregation ("sim: prec. only") compared with experimental ("XRF") values. The dashed horizontal line describes the minimum detectable density, below which the precipitates are too sparse for a single precipitate to be detected within the mapped area.

including both segregation- and precipitation-based gettering, as well as using only the precipitation model and omitting the segregation effect. The bulk [Fe_i] results for these two simulation approaches, as well as the experimental values are shown in Fig. 5, and the size distributions are similarly shown in Fig. 6.
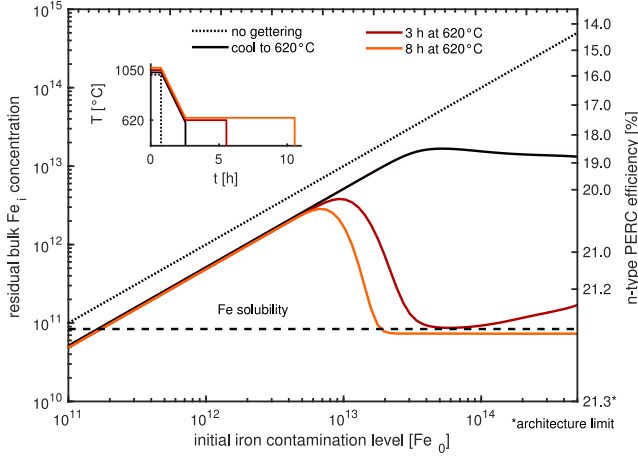
Fig. 7.   Simulated residual bulk [Fe$_i$] values for the four processes including the same implant parameters (dose, energy, and high-temperature anneal) than experimentally studied with a post-implantation 4 °C/min ramp to 620 °C followed by (a) pullout at 620 °C ("cool to 620 °C"), (b) 3 h anneal at 620 °C ("3 h at 620 °C") or (c) 8 h anneal at 620 °C ("8 h at 620 °C"). The inset describes the time-temperature profile of each process and the left axis the simulated efficiency limit imposed by the residual bulk [Fe$_i$] on a 21.3% efficient n-type PERC architecture [64]. An industrial wafer thickness of 160 μm was used in these simulations. The black dashed line the iron solubility at 620 °C and the black dotted line the residual [Fe$_i$] value assuming no gettering occurs during the process ([Fe$_i$] = [Fe$_0$]).

Overall, the most interesting feature of the simulation results is the fact that there is very little difference between the two modeling approaches. The fact that the relative effect of including or excluding the segregation effect is so small implies that precipitation is the dominant gettering mechanism under these experimental conditions, which is consistent with previous iron gettering simulations in silicon with high-energy (>100 keV) boron-implants with similar iron contamination levels as here [15]. Fig. 5 shows that despite the [Fe$_i$] concentrations varying at most by almost four orders of magnitude as a result of the gettering anneals, the results produced by the two simulation approaches are always to within a factor of two. This relative difference is comparable to, or smaller, than the uncertainty associated with the simulated or experimental results (cf., Fig. 2).

The simulated precipitate size distributions exhibit similarly minor relative differences between the two models. Because the segregation effect leaves less iron to precipitate, including the segregation model tends to favor slightly smaller precipitate sizes. The experimentally observed precipitates tend to be smaller than the simulated precipitates, which could be an indication that segregation gettering is indeed active, albeit plays a smaller role.

Although precipitation-based gettering is dominant in our experimental setup, that is not generally always the case. The good agreement between our simulation and experiments in the high-iron regime provides validation of the precipitation parameters necessary for simulation. In Fig. 7, we extend the simulations to show the residual bulk [Fe$_i$] values under different iron contamination levels for industrial 160 μm thick wafers assuming the same implant parameters (dose, energy, and high-temperature anneal) as experimentally studied here with a

post-implantation 4 °C/min ramp to 620 °C followed by a) pull-out at 620 °C ("cool to 620 °C"), b) 3 h anneal at 620 °C ("3 h at 620 °C") or c) 8 h anneal at 620 °C ("8 h at 620 °C"). Both segregation- and precipitation-based gettering are active in these simulations.

At low-to-moderate contamination levels ([Fe$_0$] < 10^{13} cm^{-3}), bulk [Fe$_i$] is reduced by approximately 50% due to segregation gettering. In this low-iron regime, the 3 or 8 h anneals at 620 °C bring no additional benefit in gettering efficiency, because the 4 °C/min ramp is slow enough to allow enough iron to diffuse to the emitter for the FeB-pairing reaction [28] to reach equilibrium.

At higher initial iron concentrations ([Fe$_0$] > 10^{13} cm^{-3}), the supersaturation required for precipitation to occur is reached, and precipitation-based gettering improves the gettering efficiency dramatically. The specific cut-off when precipitation-based gettering begins to dominate varies based on the implantation and gettering parameters chosen, but it is unlikely to occur under industrially relevant parameters for iron contamination levels below 10^{12} cm^{-3}. For precipitation-based gettering, the precipitates need to nucleate and grow. For this reason, a subsequent anneal can be significant for reaching thermal equilibrium and enhancing gettering. With the 3 h anneal at 620 °C, the simulated postgettering [Fe$_i$] comes close to the solid solubility of iron with [Fe$_0$] values above 3 × 10^{13} cm^{-3}. In this regime, the postgettering [Fe$_i$] is low enough to enable >21% efficient architecture limit of n-type Passivated Emitter and Rear Cell (PERC) devices [64]. With 160 μm thick wafers, the additional gettering efficiency brought by the 8 h anneal compared is minor compared with the 3 h anneal. Although the 3 h anneal imposes a low-throughput for the process, the kinetics could be improved by increasing the ramp rate between the implantation and gettering anneals [35]. Additional gettering efficiency may also be gained at low contamination levels from iron point defects trapping to, rather than precipitating at, dislocations [65].

Lastly, as an interesting area of future research, we highlight that the implantation defect profile, and thus the on-set off precipitation-based gettering, likely depends on the specific boron-implantation technique used. While the boron-implants of this study were performed with mass-analyzed beamline ion-implanter, promising work is ongoing to develop higher throughput ion-implant devices without mass-analysis [66], [67]. Although the dislocation distribution may differ with these new ion-implant techniques, the end-to-end model from defect generation to impurity gettering presented here should still be valid.

VI. CONCLUSION

We performed a quantitative test of the gettering induced by PV-typical boron-implants under different gettering anneals toward facilitating cost-effective manufacturing of boron-implanted silicon solar cells. We measured the bulk iron point defect concentration via diffusion length measurements as well as the iron precipitate size distribution in the implanted layer via synchrotron-based Nano-XRF. We showed that iron precipitation in the implanted layer can effectively reduce the bulk iron point defect concentration by more than 99.9% depending on

the gettering conditions. Additionally, we simulated the specific implantation damage distribution and modeled these defects as the heterogeneous precipitation sites available to iron point defects. The gettering model reproduced, to within the accuracy of the experiments and the model, the experimental bulk iron point defect concentrations in all samples and the precipitate size distributions in the implanted layer for two out of three measured samples.

Our physics-based implant gettering model can be used to quantify the expected gettering for a broad range of ion-implant parameters for both boron- and phosphorus-implantation. The model is expected to aide in the design of cost-efficient iron gettering strategies for both boron- and phosphorus-implanted silicon solar cells. In particular, the model can be used to evaluate tradeoffs between the higher efficiency achievable with improved gettering and an extended process duration. After accounting for the different diffusivity and solubility of different transition metals our model is likely to be generalizable to other common impurities, such as Cr, Ni, Cu, [68]–[71] in silicon solar cell manufacturing.

APPENDIX A
DETAILS OF GETTERING MODEL

The implantation damage model, described thoroughly in a previous report [52], calculates the average areal dislocation loop density N_L (in cm^{-2}) and the mean loop radius r_L, using the implantation parameters and the time-temperature profile as inputs. For the implantation parameters used in this study, the simulated loop density was 2.0×10^7 cm^{-2} and the average loop radius was 305.6 nm. The density and radius of the dislocation loops are then used as the density and capture radius, respectively, of precipitation sites for iron. The heterogeneous precipitation model is based on the Fokker–Planck equation and was first introduced in [53], and is also discussed, for example, in [62]. It accounts for the growth of the precipitate capture radius, $r(n)$ as a function of precipitate size [15], [71]:

$$r(n) = r_L + 5.1 \text{ nm} \times n^{1/2}$$

where *n* is the number of Fe atoms per precipitate.

The precise depth distribution of the implantation damage is unknown, but it is generally much closer to the surface than the junction depth [52]. As long as the areal density of dislocations is held constant, the dislocations can be distributed arbitrarily along the first 10–1000 nm of the wafer without changing the simulation results presented here. For comparison between the experimental and simulated size distribution, the precipitate size distribution is averaged over the full implantation damage region.

The simulation domain is one dimensional with iron initially in a dissolved state spread homogenously. No precipitation sites beyond the emitter are assumed anywhere else in the simulation domain. The precipitation model includes a lumped energy parameter E_a, which accounts for changes in precipitate surface energy and matrix strain during precipitate growth [71], and is not adjusted from previous work [35]. Iron solubility, C_S, above 700 °C is modeled as in [54], and below 700 °C as in [55].

TABLE SI
MEASURED PRECIPITATE SIZES

Sample	Precipitate sizes (Fe atoms/precipitate)
High Fe 750 °C	4.8×10^7, 1.8×10^7, 1.7×10^7, 3.5×10^7
High Fe 620 °C	5.8×10^5, 1.1×10^6, 6.8×10^6, 3.0×10^5, 1.1×10^7, 2.4×10^6, 4.0×10^5, 1.0×10^6, 5.1×10^5, 3.2×10^5, 1.4×10^7
Low Fe 620 °C	5.1×10^5, 7.2×10^5, 2.7×10^6, 4.8×10^5, 1.2×10^6, 5.1×10^5, 1.1×10^6, 2.4×10^6, 1.5×10^6, 2.8×10^6, 2.6×10^6, 1.2×10^6, 8.0×10^5, 1.4×10^6, 3.4×10^6, 4.3×10^6, 6.2×10^6, 4.6×10^5

The boron segregation model, on the other hand, describes positive interstitial iron atoms pairing with negative boron atoms [28]. The ratio of neutral and positive interstitial iron atoms is described by the Fermi level and the position of the iron donor level [72]. The ratio of paired and unpaired positive iron atoms are given by an equilibrium reaction [73], [74]. The diffusivity of iron as a function of boron concentration is modeled as in [75] and the diffusivity of intrinsic silicon is taken as in [76]. The boron profile used in the simulations is measured by the electrochemical capacitance–voltage technique, and is reported in [46].

APPENDIX B
MEASURED PRECIPITATE SIZES

To facilitate accurate further analysis of our results, the quantified precipitate sizes are listed for each individual precipitate in Table SI.

REFERENCES

[1] S. Riepe *et al.*, "Research on efficiency limiting defects and defect engineering in silicon solar cells – Results of the German research cluster solarfocus," *Phys. Status Solidi C*, vol. 8, pp. 733–738, 2011.

[2] A. Goodrich *et al.*, "A wafer-based monocrystalline silicon photovoltaics road map: Utilizing known technology improvement opportunities for further reductions in manufacturing costs," *Sol. Energy Mater. Sol. Cells*, vol. 114, pp. 110–135, 2013.

[3] F. Schindler *et al.*, "Potential gain in multicrystalline silicon solar cell efficiency by n-type doping," *IEEE J. Photovolt.* vol. 5, no. 2, pp. 499–506, Mar. 2015.

[4] M. Rüdiger, H. Steinkemper, M. Hermle, and S. W. Glunz, "Numerical current density loss analysis of industrially relevant crystalline silicon solar cell concepts," *IEEE J. Photovolt.*, vol. 4, no. 2, pp. 533–539, Mar. 2014.

[5] K. Yoshikawa *et al.*, "Silicon heterojunction solar cell with interdigitated back contacts for a photoconversion efficiency over 26%," *Nature Energy*, vol. 2, 2017, Art. no. 17032.

[6] A. Richter *et al.*, "n-Type Si solar cells with passivating electron contact: Identifying sources for efficiency limitations by wafer thickness and resistivity variation," *Sol. Energy Mater. Sol. Cells*, vol. 73, pp. 96–105, 2017.

[7] Y.-W. Ok *et al.*, "Ion-implanted and screen-printed large area 20% efficient n-type front junction Si solar cells," *Sol. Energy Mater. Sol. Cells*, vol. 123, pp. 92–96, 2014.

[8] F. Kiefer *et al.*, "Influence of the boron emitter profile on VOC and JSC losses in fully ion implanted n-type PERT solar cells," *Phys. Status Solidi A*, vol. 212, pp. 291–297, 2015.

[9] A. Rohatgi *et al.*, "High-throughput ion-implantation for low-cost high-efficiency silicon solar cells," *Energy Procedia*, vol. 15, pp. 10–19, 2012.

[10] V. Prajapati T. Janssens, J. John, J. Poortmans, and R. Mertens, "Diffusion-free high efficiency silicon solar cells," *Prog. Photovolt. Res. Appl.*, vol. 21, pp. 980–985, 2013.

[11] A. A. Istratov, H. Hieslmair, and E. R. Weber, "Iron contamination in silicon technology," *Appl. Phys. A*, vol. 70, pp. 489–534, 2000.

[12] G. Zoth, and W. Bergholz, "A fast, preparation-free method to detect iron in silicon," *J. Appl. Phys.*, vol. 67, pp. 6764–6771, 1990.

[13] D. H. Macdonald, L. J. Geerligs, and A. Azzizi, "Iron detection in crystalline silicon by carrier lifetime measurements for arbitrary injection and doping," *J. Appl. Phys.*, vol. 95, pp. 1021–1028, 2004.

[14] E. R. Weber, "Transition metals in silicon," *Appl. Phys. A*, vol. 30, pp. 1–22, 1983.

[15] A. Haarahiltunen *et al.*, "Gettering of iron in silicon by boron implantation," *J. Mater. Sci. Mater. Electron.*, vol. 19, pp. 41–45, 2008.

[16] M. I. Asghar *et al.*, "Competitive iron gettering between internal gettering sites and boron implantation in CZ-silicon," *Mater. Sci. Eng. B*, vol. 159, pp. 224–227, 2009.

[17] J. L. Benton *et al.*, "The mechanisms of iron gettering in silicon by boron ion-implantation," *J. Electrochem. Soc.*, vol. 143, pp. 1406–1409, 1996.

[18] S. M. Myers *et al.*, "Metal gettering by boron-silicide precipitates in boron-implanted silicon," *Nucl. Instrum. Methods Phys. Res. B*, vol. 127, pp. 291–296, 1997.

[19] T. Terakawa, D. Wang, and H. Nakashima, "Role of heavily B-doped layer on low-temperature Fe gettering in bifacial Si solar cell fabrication," *Jpn. J. Appl. Phys.*, vol. 45, pp. 2643–2647, 2006.

[20] J. Schön, M. C. Schubert, W. Warta, H. Savin, and A. Haarahiltunen, "Analysis of simultaneous boron and phosphorus diffusion gettering in silicon," *Phys. Status Solidi A*, vol. 207, pp. 2589–2592, 2010.

[21] V. Vähänissi *et al.*, "Physical mechanisms of boron diffusion gettering of iron in silicon," *Phys. Status Solidi RRL*, vol. 4, pp. 136–138, 2010.

[22] H. Talvitie, V. Vähänissi, A. Haarahiltunen, M. Yli-Koski, and H. Savin, "Phosphorus and boron diffusion gettering of iron in monocrystalline silicon," *J. Appl. Phys.*, vol. 109, 2011, Art. no. 093505.

[23] S. P. Phang and Daniel Macdonald, "Effect of boron codoping and phosphorus concentration on phosphorus diffusion gettering," *IEEE J. Photovolt.*, vol. 4, no. 1, pp. 64–69, Jan. 2014.

[24] S. P. Phang, W. Liang, B. Wolpensinger, M. A. Kessler, and D. Macdonald, "Tradeoffs between impurity gettering, bulk degradation, and surface passivation of Boron-Rich layers on silicon solar cells," *IEEE J. Photovolt.*, vol. 3, no. 1, pp. 261–266, Jan. 2013.

[25] S. P. Phang and D. Macdonald, "Direct comparison of boron, phosphorus, and aluminum gettering of iron in crystalline silicon," *J. Appl. Phys.*, vol. 109, 2011, Art. no. 073521.

[26] J. L. Benton *et al.*, "Iron gettering mechanisms in silicon," *J. Appl. Phys.*, vol. 80, pp. 3275–3284, 1996.

[27] M. Miyazaki *et al.*, "Efficiency of boron gettering for iron impurities in p/p+ epitaxial silicon wafers," *Jpn. J. Appl. Phys.*, vol. 36, pp. L380–L381, 1997.

[28] H. Hieslmair, A. A. Istartov, C. Flink, S. A. McHugo, and E. R. Weber, "Experiments and computer simulations of iron profiles in p/p+ silicon: Segregation and the position of the iron donor level," *Phys. B Condens. Matter*, vol. 273, pp. 441–444, 1999.

[29] K. S. Jones, S. Prussin, and E. R. Weber, "A systematic analysis of defects in ion-implanted silicon," *Appl. Phys. A*, vol. 45, pp. 1–34, 1988.

[30] J. Krügener *et al.*, "Electrical and structural analysis of crystal defects after high-temperature rapid thermal annealing of highly boron ion-implanted emitters," *IEEE J. Photovolt.*, vol. 5, no. 1, pp. 166–173, Jan. 2015.

[31] S. Tian *et al.*, "A detailed physical model for ion implant induced damage in silicon," *IEEE Trans. Electron. Dev.*, vol. 45, no. 6, pp. 1226–1238, Jun. 1998.

[32] R. A. Brown, O. Kononchuk, and G. A. Rozgonyi, "Simulation of metallic impurity gettering in silicon by MeV ion implantation," *Nucl. Instrum. Methods Phys. Res. B*, vol. 148, pp. 322–328, 1999.

[33] T. Kuroi *et al.*, "Proximity gettering of heavy metals by high-energy ion implantation," *Jpn. J. Appl. Phys.*, vol. 32, pp. 303–307, 1993.

[34] G. V. Gadiyak, "Dislocation formation and gettering mechanism of impurity atoms close to the active region," *Nucl. Instrum. Methods Phys. Res. B*, vol. 127, pp. 252–255, 1997.

[35] H. S. Laine *et al.*, "Impact of iron precipitation on phosphorus-implanted silicon solar cells," *IEEE J. Photovolt.*, vol. 6, no. 5, pp. 1094–1102, Sep. 2016.

[36] A. Haarahiltunen, H. Väinölä, O. Anttila, M. Yli-Koski, and J. Sinkkonen, "Experimental and theoretical study of heterogeneous iron precipitation in silicon," *J. Appl. Phys.*, vol. 101, 2007, Art. no. 043507.

[37] D. P. Fenning *et al.*, "Precipitated iron: A limit on gettering efficacy in multicrystalline silicon," *J. Appl. Phys.*, vol. 113, 2013, Art. no. 044521.

[38] J. Hofstetter *et al.*, "Impurity-to-efficiency simulator: predictive simulation of silicon solar cell performance based on iron content and distribution," *Prog. Photovolt. Res. Appl.*, vol. 19, pp. 487–497, 2011.

[39] J. Schön *et al.*, "Main defect reactions behind phosphorus diffusion gettering of iron," *J. Appl. Phys*, vol. 116, 2015, Art. no. 244503.

[40] H. Hieslmair, S. Balasubramanian, A. A. Istratov, and E. R. Weber, "Gettering simulator: Physical basis and algorithm," *Semicond. Sci. Technol.*, vol. 16, pp. 567–574, 2001.

[41] M. Syre, S. Karazhanov, B. R. Olaisen, A. Holt, and B. G. Svensson, "Evaluation of possible mechanisms behind P gettering of iron," *J. Appl. Phys.*, vol. 110, 2011, Art. no. 024912.

[42] R. Chen, B. Trzynadlowski, and S. T. Dunham, "Phosphorus vacancy cluster model for phosphorus diffusion gettering of metals in Si," *J. Appl. Phys.*, vol. 115, 2014, Art. no. 054906.

[43] A. E. Morishige *et al.*, "Synchrotron-based investigation of transition-metal getterability in n-type multicrystalline silicon," *Appl. Phys. Lett.*, vol. 108, 2016, Art. no. 202104.

[44] V. Vähänissi, A. Haarahiltunen, M. Yli-Koski, and H. Savin, "Gettering of iron in silicon solar cells with implanted emitters," *IEEE J. Photovolt.*, vol. 4, no. 1, pp. 142–147, Jan. 2014.

[45] V. Vähänissi, A. Haarahiltunen, H. Talvitie, M. Yli-Koski, and H. Savin, "Impact of phosphorus gettering parameters and initial iron level on silicon solar cell properties," *Prog. Photovolt. Res. Appl.*, vol. 21, pp. 1127–1135, 2013.

[46] G. von Gastrow *et al.*, "Recombination processes in passivated boron-implanted black silicon emitters," *J. Appl. Phys.*, vol. 121, 2017, Art. no. 185706.

[47] H. Vahlman *et al.*, "Modeling of light-induced degradation due to Cu precipitation in p-type silicon. II. Comparison of simulations and experiments," *J. Appl. Phys.*, vol. 121, 2017, Art. no. 195704.

[48] A. Y. Liu *et al.*, "Gettering of interstitial iron in silicon by plasma-enhanced chemical vapour deposited silicon nitride films," *J. Appl. Phys.*, vol. 120, 2016, Art. no. 193103.

[49] A. Y. Liu and D. Macdonald, "Impurity gettering effect of atomic layer deposited aluminium oxide films on silicon wafers," *Appl. Phys. Lett.*, vol. 110, 2017, Art. no. 191604.

[50] A. Haarahiltunen, H. Väinölä, M. Yli-Koski, J. Sinkkonen, and O. Anttila, "Modeling and optimization of internal gettering of iron in silicon," *ECS Trans.*, vol. 3, pp. 273–284, 2006.

[51] A. E. Morishige *et al.*, "Increased throughput and sensitivity of synchrotron-based characterization for photovoltaic materials," *IEEE J. Photovolt.*, vol. 7, no. 3, pp. 763–771, May 2017.

[52] F. A. Wolf, A. Martinez-Limia, D. Stichtenoth, and P. Pichler, "Modeling the annealing of dislocation loops in implanted c-Si solar cells," *IEEE J. Photovolt.*, vol. 4, no. 3, pp. 851–858, May 2014.

[53] A. Haarahiltunen, H. Väinölä, O. Anttila, M. Yli-Koski, and J. Sinkkonen, "Experimental and theoretical study of heterogeneous iron precipitation in silicon," *J. Appl. Phys.*, vol. 101, 2007, Art. no. 043507.

[54] M. Aoki, H. Akito, and O. Akira, "Fundamental properties of intrinsic gettering of iron in a silicon wafer," *J. Appl. Phys.*, vol. 72, pp. 895–898, 1992.

[55] J. D. Murphy and R. J. Falster, "Contamination of silicon by iron at temperatures below 800 °C," *Phys. Status Solidi RRL*, vol. 5, pp. 370–372, 2011.

[56] H. S. Laine *et al.*, "Toward effective gettering in boron-implanted silicon solar cells," in *Proc. 44th IEEE Photovolt. Spec. Conf.*, Washington, DC, USA, Jun. 2017, to be published.

[57] A. Hähnel *et al.*, "Electron microscope verification of prebreakdown-inducing α-FeSi$_2$ needles in multicrystalline silicon solar cells," *J. Appl. Phys.*, vol. 113, 2013, Art. no. 044505.

[58] O. Breitenstein, J. P. Rakotoniaina, M. H. Al Rifai, and M. Werner, "Shunt types in crystalline silicon solar cells," *Prog. Photovolt. Res. Appl.*, vol. 12, pp. 529–538, 2004.

[59] T. Buonassisi *et al.*, "Observation of transition metals at shunt locations in multicrystalline silicon solar cells," *J. Appl. Phys.*, vol. 95, pp. 1556–1561, 2004.

[60] J.-F. Lelièvre *et al.*, "Dissolution and gettering of iron during contact co-firing," *Energy Procedia*, vol. 8, pp. 257–262, 2011.

[61] B. Michl, J. Schön, W. Warta, and M. C. Schubert, "The impact of different diffusion temperature profiles on iron concentrations and carrier lifetimes in multicrystalline silicon wafers," *IEEE J. Photovolt.*, vol. 3, no. 2, pp. 635–640, Apr. 2013.

[62] A. E. Morishige *et al.*, "Building intuition of iron evolution during solar cell processing through analysis of different process models," *Appl. Phys. A*, vol. 120, pp. 1357–1373, 2015.

[63] D. P. Fenning *et al.*, "Improved iron gettering of contaminated multicrystalline silicon by high-temperature phosphorus diffusion," *J. Appl. Phys.*, vol. 113, 2013, Art. no. 214504.

[64] J. Schmidt *et al.*, "Impurity-related limitations of next-generation industrial silicon solar cells," *IEEE J. Photovolt.*, vol. 3, no. 1, pp. 114–118, Jan. 2013.

[65] A. Yazdani, R. Chen, and S. T. Dunham, "Coupled modeling of the competitive gettering of transition metals and impact on performance of lifetime sensitive devices," *J. Appl. Phys.*, vol. 121, 2017, Art. no. 095702.

[66] D. L. Young *et al.*, "Plasma immersion ion implantation for interdigitated back passivated contact (IBPC) solar cells," in *Proc. 43rd IEEE Photovolt. Spec. Conf. Rec.*, 2016, pp. 0225–0229.

[67] J.-F. Lerat *et al.*, "Boron emitter formation by plasma immersion ion-implantation in n-type PERT silicon solar cells," *Energy Procedia*, vol. 92, pp. 697–701, 2016.

[68] M. Jensen *et al.*, "Solubility and diffusivity: Important metrics in the search for the root cause of LeTID," submitted for publication.

[69] J. Schön, H. Habenicht, W. Warta, and M. C. Schubert, "Chromium distribution in multicrystalline silicon: Comparison of simulations and experiments," *Prog. Photovolt. Res. Appl.*, vol. 21, pp. 676–680, 2013.

[70] M. A. Jensen *et al.*, "Synchrotron-based analysis of chromium distributions in multicrystalline silicon for solar cells," *Appl. Phys. Lett.*, vol. 106, 2015, Art. no. 202104.

[71] S. T. Dunham, "Growth kinetics of disk-shaped extended defects with constant thickness," *Appl. Phys. Lett.*, vol. 63, pp. 464–466, 1993.

[72] A. A. Istratov, H. Huber, and E. R. Weber, "Modeling of competitive gettering of iron in silicon integrated circuit technology," *J. Electrochem. Soc.*, vol. 150, pp. G244–G252, 2003.

[73] H. Lemke, "Energieniveaus und Bindungsenergien von Ionenpaaren in Silizium," *Phys. Status Solidi A*, vol. 76, pp. 223–234, 1983.

[74] L. C. Kimerling and J. L. Benton, "Electronically controlled reactions of interstitial iron in silicon," *Physica B+C*, vol. 116, pp. 297–300, 1983.

[75] A. Haarahiltunen, "Heterogeneous precipitation and internal gettering efficiency of iron in silicon," Ph.D. dissertation, Helsinki Univ. Technol., Espoo, Finland, 2007.

[76] A. A. Istratov, H. Hieslmair, and E. R. Weber, "Iron and its complexes in silicon," *Appl. Phys. A*, vol. 69, pp. 13–44, 1999.

Hannu S. Laine received the B.sc. and M.Sc. degrees from Aalto University, Espoo, Finland, in 2014 and 2015, respectively, majoring in engineering physics and advanced energy systems. He is currently working toward the Ph.D. degree in electrical engineering at Aalto University.

He was a visiting Fulbright Technology Industry of Finland Researcher at Massachusetts Institute of Technology for the academic year 2015–2016. His research focuses on characterizing and mitigating detrimental metal impurities in silicon solar cells.

Ville Vähänissi received the D.Sc. (Tech.) degree in semiconductor technology from Aalto University, Espoo, Finland, in 2016.

He is currently working as a Staff Scientist in the Department of Electronics and Nanoengineering, School of Electrical Engineering, Aalto University. His research interests include defect engineering in silicon, especially photovoltaics, as well as atomic layer deposition and its various applications in semiconductor devices.

Zhengjun Liu received the M.Sc. degree from Aalto University, Espoo, Finland, in 2012, majoring in micro- and nanotechnology. She is currently working toward the Ph.D. degree in the same field.

Her research interests include the defect engineering of silicon materials for photovoltaic applications and fabrication process development for silicon-based devices.

Ernesto Magaña received the B.S. and M.S. degrees in nanoengineering from the University of California, San Diego, CA, USA, in 2015 and 2017, respectively.

As a Graduate Researcher, his work focused on silicon materials engineering for use in solar cells with a primary focus on low-temperature doping and characterization of metal impurities and structural defects. He is currently employed as a Process Technology Development Engineer at Intel.

Jan Krügener received the Diploma and Ph.D. degrees in electrical engineering from Leibniz Universität Hannover, Hannover, Germany, in 2008 and 2012, respectively.

He is an Associate Researcher at the Institute of Electronic Materials and Devices, Leibniz Universität Hannover. His research interests include fabrication and characterization of advanced high-efficiency silicon solar cells.

Ashley E. Morishige received the Bachelor of Engineering degree from Thayer School of Engineering at Dartmouth, Hanover, NH, USA, in 2011, and the M.S. and Ph.D. degrees in mechanical engineering from the Massachusetts Institute of Technology (MIT), Cambridge, MA, USA, in 2013 and 2016, respectively.

She was a Postdoctoral Researcher in the Photovoltaic Research Laboratory, MIT, until she joined 1366 Technologies Inc., Bedford, MA, as a Process Development Engineer, in 2016.

Kristian Salo is currently working toward the B.Sc. degree in electrical engineering at Aalto University, Espoo, Finland.

During 2016, he was a Research Assistant at Professor Hele Savin's group, Aalto University, where he participated in research projects investigating defect engineering, surface passivation, and light-induced degradation in silicon photovoltaics.

Barry Lai received the Ph.D. degree in physics from the University of Wisconsin-Madison, Madison, WI, USA, in 1990.

He currently leads the X-ray fluorescence microprobe Beamline 2-ID-D at the Advanced Photon Source, which is the synchrotron facility at Argonne National Laboratory, Argonne, IL, USA. He is interested in imaging and characterization of energy materials and systems (batteries, fuel cells, photovoltaics, catalysts) using X-ray microscopy techniques. In particular, he is developing *in situ* applications and sample environments appropriate for microscopy studies.

David P. Fenning received the Ph.D. degree in mechanical engineering from Massachusetts Institute of Technology, Cambridge, MA, USA, working on silicon solar cell materials engineering, in 2013.

After working with the R&D team at 1366 Technologies Inc., he was an MIT/Battelle Postdoctoral Fellow in solar fuels. He currently focuses on defects and reliability in silicon and hybrid perovskite solar cells and CO_2 electrocatalysis for solar fuels. He is an Assistant Professor in nanoengineering at the University of California, San Diego, CA, USA, where his group researches materials for solar energy conversion and storage.

Hele Savin received the D.S. (Tech.) degree in semiconductor technology from Aalto University, Espoo, Finland, in 2005.

Her research interests include material research in semiconductors, more specifically defect engineering in silicon, nanostructured silicon, light-induced degradation, and silicon photodetectors. She is currently an Associate Professor in the Department of Micro and Nanosciences, Aalto University.